Journal of Electronics and Electrical Engineering
https://ojs.wiserpub.com/index.php/JEEE/

Article

Numerical Simulation of Electro-Thermal Properties in FDSOI MOSFETs Down to Deep Cryogenic Temperatures

Gerard Ghibaudo* **and Francis Balestra**

IMEP-LAHC, Univ. Grenoble Alpes, Minatec, 38016 Grenoble, France
E-mail: gerard.ghibaudo@grenoble-inp.fr

Received: 14 February 2023; **Revised:** 3 April 2023; **Accepted:** 4 April 2023

Abstract: An original reformulation of the thermopower *S*, heat conductivity *K* and heat capacitance *C* in bulk silicon for electrons and phonons is first proposed. Closed-form analytical approximations for these coefficients as a function of Fermi level, temperature and/or carrier concentration are developed for implementation in TCAD simulation. These analytical expressions for *S*, *K* and *C* have been employed to simulate the electro-thermal properties of a FDSOI (Fully depleted silicon on insulator) MOSFET versus front gate voltage from room down to very low temperature. The obtained results allow discriminating the electron and phonon contributions to the whole properties. These analyses could be very useful to further performing TCAD simulations of FDSOI MOSFETs down to very low temperature for full assessment of electro-thermal performances.

Keywords: thermopower, thermal conductivity, heat capacitance, phonon drag, TCAD simulation, MOSFET, FDSOI, cryogenic temperature

1. Introduction

The cryogenic microelectronics is still a crucial research subject as allowing circuit performance enhancements in terms of operation speed, turn-on behavior, thermal noise reduction, punch-through decrease [1–9]. It can be used in many fields of application such as high speed computing, detection and sensing, spatial electronics and lately in readout CMOS electronics and quantum-bit MOS devices for quantum computing [10,11]. In this context, there are many challenges in characterization and modelling of MOS devices down to deep cryogenic temperatures. Recently, efforts have been made for achieving TCAD device simulations down to deep cryogenic temperatures [12–14]. However, electro-thermal numerical simulations are still missing and are very challenging to be performed down to very low temperatures. They could bring paramount information about the electro-thermal properties such as electronic conductivity, thermopower, Peltier coefficient and thermal conductivity of MOS devices operated down to sub Kelvin temperature and further used for instance in self-heating simulation.

Therefore, in this work, we first aim at developing original reformulations of thermopower, heat conductivity and heat capacitance for electrons and phonons in bulk silicon as a function of Fermi level position, temperature and/or carrier concentration, as well as closed-form analytical approximations useful for TCAD simulation. Then, these approximations are used for the assessment by numerical simulations of electro-thermal performances of FDSOI (Fully depleted silicon on insulator) MOSFETs operated down to very low temperatures (100mK). These results will constitute a first step to further 2D/3D TCAD simulations of electro-thermal properties (transport, self-heating…) in FDSOI MOSFETs at deep cryogenic temperatures.

Copyright ©2023 Gerard Ghibaudo, et al.
DOI: https://doi.org/10.37256/jeee.2120232498
This is an open-access article distributed under a CC BY license
(Creative Commons Attribution 4.0 International License)
https://creativecommons.org/licenses/by/4.0/

2. Theoretical Background

In this section, we first reformulate in an original way the electronic parameters such as the electronic thermopower S_e, the electronic heat conductivity K_e and the electronic heat capacitance C_e needed for the simulation of the channel properties in a FDSOI MOSFET. We also recall the phonon-related parameters such as the phonon heat capacitance C_{ph}, the phonon heat conductivity K_{th} and the phonon drag thermopower S_{ph} necessary for a complete simulation of charge and heat transport. To this end, we also establish closed-form analytical approximations of the thermal and transport coefficients useful for TCAD simulation.

2.1 *Electronic Parameters*

The electron concentration in a bulk semiconductor is obtained from the Fermi-Dirac statistics as [15],

$$n = N_C(T) \cdot \frac{2}{\sqrt{\pi}} \cdot F_{1/2}(u_f) \tag{1}$$

where $N_C(T)$ is the effective density of states ($= 2\times10^{19} \cdot \left(\frac{T}{300}\right)^{\frac{3}{2}}$ for silicon) and $F_{1/2}(u_f)$ is the Fermi-Dirac integral defined as [15],

$$F_{1/2}(u_f) = \int_0^{\infty} \frac{u^{1/2}}{1+\exp(u-u_f)} du \tag{2}$$

where $u = E/kT$ is the reduced energy and $u_f = E_F/kT$ the reduced Fermi energy, kT being the thermal energy. The conduction band edge E_c is herein referenced to zero.

The electronic conductivity σ calculated within the Kubo-Greenwood formalism is expressed as [16,17],

$$\sigma = \int_0^{+\infty} \sigma_E(E) \cdot \left(-\frac{\partial f}{\partial E}\right) dE \tag{3}$$

where $f = 1/\left(1+e^{\frac{E-E_f}{kT}}\right)$ is the Fermi distribution function and $\sigma_E(E)$ is the energy conductivity function given by,

$$\sigma_E(E) = \frac{2}{3} q \cdot E \cdot N(E) \cdot \mu(E) \tag{4}$$

with q being the electronic charge, E the carrier kinetic energy, $N(E) \sim E^{1/2}$ the 3D density of states and $\mu(E)$ the energy mobility function.

The electronic thermoelectric power (or Seebeck coefficient) S_e is then obtained in the form [16,18],

$$S_e = \frac{k}{q} \cdot \frac{\int_0^{+\infty} \sigma_E(E) \cdot \left(\frac{E-E_f}{kT}\right) \cdot \left(-\frac{\partial f}{\partial E}\right) dE}{\int_0^{+\infty} \sigma_E(E) \cdot \left(-\frac{\partial f}{\partial E}\right) dE} \tag{5}$$

Likewise, the electronic heat conductivity K_e can be expressed as [18],

$$K_e = T \cdot \left(\frac{k}{q}\right)^2 \cdot \int_0^{+\infty} \sigma_E(E) \cdot \left(\frac{E-E_f}{kT}\right)^2 \cdot \left(-\frac{\partial f}{\partial E}\right) dE \tag{6}$$

Similarly, the electronic heat capacitance $C_e = \partial U_e / \partial T$, U_e being the electronic energy, can be equated to as [19],

$$C_e = \frac{\partial U_e}{\partial T} = \frac{\partial \int_0^{+\infty} E \cdot N(E) \cdot f\, dE}{\partial T} = \int_0^{+\infty} E \cdot N(E) \cdot \left(\frac{\partial f}{\partial T}\right) dE \tag{7}$$

If we assume, for the sake of simplicity, a constant mobility versus energy i.e. $\mu(E) = const.$, the electronic thermopower S_e, the reduced electronic heat conductivity $K_e/(\sigma \cdot T)$ and the reduced electronic heat capacitance C_e/n can then be calculated from the integrals (5), (6) and (7) as,

$$S_e(u_f) = \frac{k}{q} \cdot \frac{\int_0^{+\infty} (u-u_f) \cdot u^{\frac{3}{2}} \cdot \frac{e^{u-u_f}}{\left(1+e^{u-u_f}\right)^2} du}{\int_0^{+\infty} u^{\frac{3}{2}} \cdot \frac{e^{u-u_f}}{\left(1+e^{u-u_f}\right)^2} du} \tag{8}$$

$$\frac{K_e}{\sigma T}(u_f) = \left(\frac{k}{q}\right)^2 \cdot \frac{\int_0^{+\infty} (u-u_f)^2 \cdot u^{\frac{3}{2}} \cdot \frac{e^{u-u_f}}{\left(1+e^{u-u_f}\right)^2} du}{\int_0^{+\infty} u^{\frac{3}{2}} \cdot \frac{e^{u-u_f}}{\left(1+e^{u-u_f}\right)^2} du} \tag{9}$$

and

$$\frac{C_e}{n}(u_f) = k \cdot \frac{\int_0^{+\infty} (u-u_f) \cdot u^{\frac{3}{2}} \cdot \frac{e^{u-u_f}}{\left(1+e^{u-u_f}\right)^2} du}{\int_0^{+\infty} u^{\frac{1}{2}} \cdot \frac{1}{\left(1+e^{u-u_f}\right)} du} \tag{10}$$

In the case of Maxwell-Boltzmann's statistics (MB) i.e. $u_f < 0$, $f \approx e^{u_f}$, so that the carrier concentration, the electronic thermopower, the reduced electronic heat conductivity and the reduced heat capacitance read respectively,

$$n \approx N_C(T) e^{u_f} \tag{11}$$

$$S_e(u_f) \approx \frac{k}{q} \cdot (2 - u_f) = \frac{k}{q} \cdot \left[2 + \ln\left(\frac{N_C(T)}{n}\right)\right] \tag{12}$$

$$\frac{K_e}{\sigma T}(u_f) \approx \left(\frac{k}{q}\right)^2 \cdot (2 - u_f)^2 = \left(\frac{k}{q}\right)^2 \cdot \left[2 + \ln\left(\frac{N_C(T)}{n}\right)\right]^2 \tag{13}$$

and

$$\frac{C_e}{n}(u_f) \approx k \cdot (3 - \frac{3}{2} u_f) = k \cdot \left[3 + \frac{3}{2} \ln\left(\frac{N_C(T)}{n}\right)\right] \tag{14}$$

In the case of degenerate (metallic) statistics (deg.), i.e. $u_f > 0$, $f = 1$ up to u_f, such that the carrier concentration, the electronic thermopower, the reduced electronic heat conductivity and the reduced heat capacitance can be obtained using the Sommerfeld expansion of the integrals (8), (9) and (10) in the form [15],

$$n \approx \frac{4}{3\sqrt{\pi}} \cdot N_C(T) \cdot u_f^{3/2} \tag{15}$$

$$S_e(u_f) \approx \frac{\pi^2}{2} \cdot \frac{k}{q} \cdot \frac{1}{u_f} = \frac{\pi^2}{2} \cdot \frac{k}{q} \cdot \left[\frac{4}{3\sqrt{\pi}} \cdot \frac{N_C(T)}{n}\right]^{2/3} \tag{16}$$

$$\frac{K_e}{\sigma T}(u_f) \approx \frac{\pi^2}{2} \cdot \left(\frac{k}{q}\right)^2 \text{(Lorenz's number)} \tag{17}$$

and

$$\frac{C_e}{n}(u_f) \approx \frac{3\pi^2}{4} \cdot k \cdot \frac{1}{u_f} = \frac{3\pi^2}{4} \cdot k \cdot \left[\frac{4}{3\sqrt{\pi}} \cdot \frac{N_C(T)}{n}\right]^{2/3} \tag{18}$$

Note that Eq. (17) translates the so-called Wiedemann–Franz law, which gives the electronic heat conductivity in metals.

In Figure 1 are reported the typical dependence of the carrier concentration with reduced Fermi energy as given by Fermi-Dirac statistics (1) as well as its Maxwell-Boltzmann limit (11) and power law degenerate metallic approximation (15).

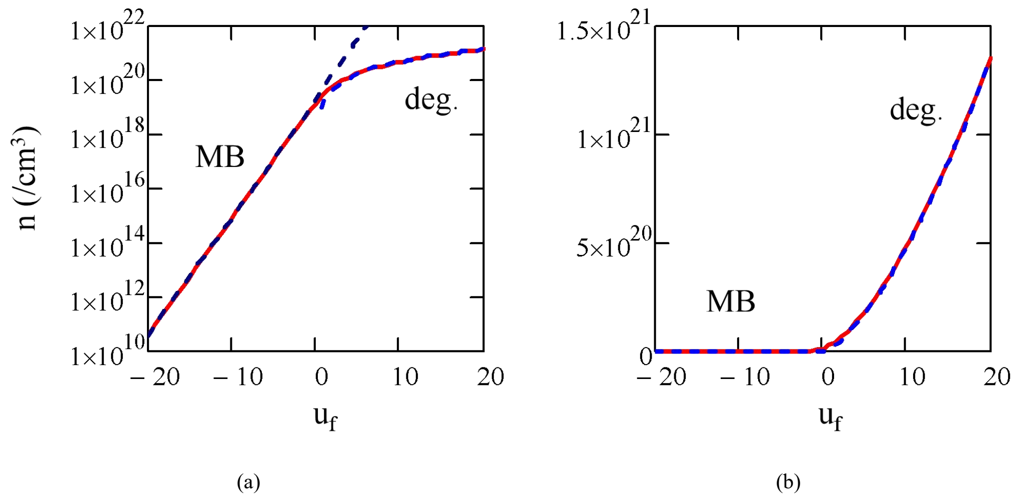

(a) (b)

Figure 1. Variations of carrier concentration *n* with reduced Fermi energy u_f in log scale (a) and linear scale (b) as obtained by Fermi-Dirac statistics (solid line), Maxwell-Boltzmann (MB) and degenerate metallic (deg.) approximations (dashed lines) (T=300K).

Figure 2 shows the corresponding variations of the electronic thermopower, the reduced electronic heat conductivity and the reduced heat capacitance with reduced Fermi energy as obtained from Fermi-Dirac statistics (8), (9) and (10), as well as their Maxwell-Boltzmann (12), (13) and (14) and degenerate (16), (17) and (18) asymptotic approximations. Both the electronic thermopower S_e, the reduced electronic heat conductivity $K_e/(\sigma \cdot T)$ and the reduced heat capacitance C_e/n strongly decrease with the reduced Fermi energy u_f i.e. also with the carrier concentration. Note that, when the Maxwell-Boltzmann statistics holds, Eqs (12) and (13) indicate that $K_e/(\sigma \cdot T) \approx S_e^2$. In the case of degenerate statistics, S_e decreases as the reciprocal reduced Fermi energy i.e. also as a power law of n (see Eq. 16), whereas the reduced electronic heat conductivity $K_e/(\sigma \cdot T)$ saturates to the so-called Lorenz number (Eq. 17) i.e. Wiedemann-Franz's law. Interestingly, examination of Eqs (12) and (14) as well as of Eqs (16) and (18) indicate that $(C_e/n)/k$ is equal to $3S_e/(2k/q)$ as confirmed by the plot of Figure 2. Actually, this original feature, which is not evident to find by direct inspection of Eqs (8) and (10), follows from the fact that $\int_0^{+\infty} u^{\frac{1}{2}} \cdot \frac{1}{\left(1+e^{u-u_f}\right)} du = \frac{2}{3} \int_0^{+\infty} u^{\frac{3}{2}} \cdot \frac{e^{u-u_f}}{\left(1+e^{u-u_f}\right)^2} du$. However, it should be mentioned that this equality between $(C_e/n)/k$ and $3S_e/(2k/q)$ is only verified because the mobility *μ(E)* was assumed constant in Eq. (5). Otherwise, $(C_e/n)/k$ and $3S_e/(2k/q)$ would slightly differ but they would keep the same trend versus u_f.

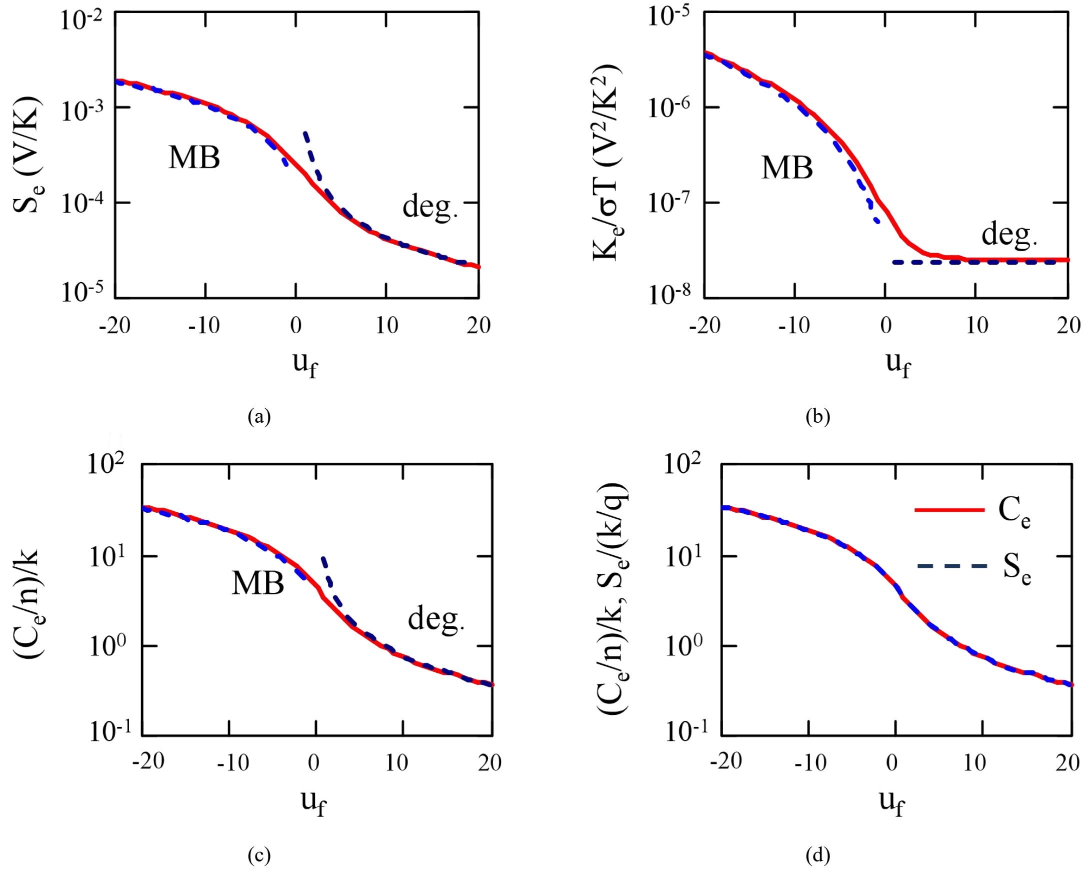

Figure 2. Variations of electronic thermopower S_e (a) and reduced electronic heat conductivity $K_e/(\sigma \cdot T)$ (b) and reduced electronic heat capacitance C_e/N (c) and $3Se/(2k/q)$ (d) with reduced Fermi energy u_f as obtained from Fermi-Dirac statistics expressions (8), (9) and (10), as well as from Maxwell-Boltzmann (12), (13) and (14) and degenerate (16), (17) and (18) asymptotic approximations (T=300K).

The equations providing the carrier concentration n, the electronic thermopower S_e, the reduced electronic conductivity $K_e/(\sigma \cdot T)$ and the reduced heat capacitance C_e/n in bulk silicon, previously depicted, are not analytical since governed by the Fermi-Dirac statistics for the whole range of reduced Fermi energy (see Eqs (1), (8), (9)and (10)). For numerical simulation purpose, it is worthwhile to establish simple analytical closed-form expressions providing accurate approximations for n, S_e, $K_e/(\sigma \cdot T)$ and C_e/n versus u_f or n over the whole carrier concentration range from semiconductor to metallic regimes.

Based on the Maxwell-Boltzmann and degenerate asymptotic limits presented above and on usual interpolation smoothing method already employed for *n,* for example in cryogenic TCAD simulations [14], it is easy to construct the following analytical expressions for n, S_e, $K_e/(\sigma \cdot T)$ and C_e/n as a function of the reduced Fermi energy,

$$n(u_f) = N_C(T) \cdot \left[\ln\left(1 + e^{\frac{2u_f}{3}}\right) \right]^{3/2} \cdot \left[1 + p + p \cdot tanh\left(\frac{u_f + 2}{2}\right) \right] \quad \text{with } p \approx 0.195 \tag{19}$$

$$S_e(u_f) = \frac{k}{q} \left\{ \left[\frac{1}{2 + \ln\left(1 + \frac{N_C(T) + 4 \cdot n(u_f)}{n(u_f)}\right)} \right]^a + \left[\frac{1}{\frac{\pi^2}{2} \cdot \left[\frac{4}{3\sqrt{\pi}} \cdot \frac{N_C(T)}{n(u_f)} \right]^{2/3}} \right]^a \right\}^{-1/a} \quad \text{with } a \approx 2 \tag{20}$$

$$\frac{K_e}{\sigma T}(u_f)=\left[\left(S_e(u_f)^2\right)^b+\left(\frac{\pi^2}{2}\cdot\left(\frac{k}{q}\right)^2\right)^b\right]^{1/b} \quad \text{with } b\approx 1.1 \tag{21}$$

and

$$\frac{C_e}{n}(u_f)=\frac{3}{2}q\cdot S_e(u_f) \tag{22}$$

It should be noted that these formulas well reduce to their Maxwell-Boltzmann and degenerate asymptotic limits for $u_f<0$ or $u_f>0$, respectively (see Eqs (12), (13) and (14) or Eqs (16), (17) and (18)). The parameters in the analytical formulas have been optimized in order to minimize the error with respect to the exact results (see below).

Figure 3a shows the variation of the carrier concentration with reduced Fermi energy as obtained from the rigorous Fermi-Dirac statistics (1) and from the analytical formula (15), both in log and linear scales. As can be seen from the figure, Eq. (19) provides a very good approximation to the exact solution with an error inferior to $\approx 5\%$ over the whole reduced Fermi energy range varying from -20 to +20 (see Figure 3b), which is quite sufficient for TCAD simulation of real devices [14].

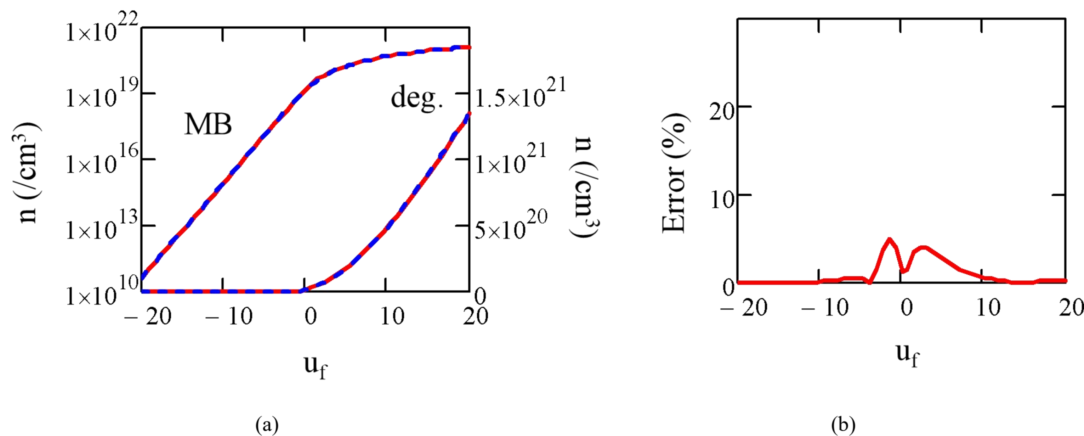

(a) (b)

Figure 3. (a) Variations of carrier concentration n with reduced Fermi energy u_f in log scale and linear scale as obtained by exact Fermi-Dirac statistics (solid lines) and by analytical approximation of Eq. (19) (dahsed lines) and (b) Variations of corresponding error.

In Figure 4 are compared the variations of the electronic thermopower S_e and of the reduced electronic heat conductivity $K_e/\sigma T$ with reduced Fermi energy u_f as calculated from the exact integrals (8) and (9) to those obtained with the analytical formulas (20) and 21). As can be seen, Eqs (20) and (21) offer very good approximations to the exact results with an overall error below $\approx 8\%$ and $\approx 12\%$, respectively, over the whole Fermi energy range (see Figure 4b) for both the thermopower S_e and reduced electronic heat conductivity $K_e/\sigma T$, with a better accuracy for S_e.

In Figure 5 are reported the variations of the reduced electronic heat capacitance C_e/n with reduced Fermi energy u_f as computed from the exact integral (10) along with those obtained with the analytical formula (22). As can also be seen, Eq. (22) gives a very good approximation to the exact result with an overall error below ≈8% over the whole Fermi energy range as for $S_e(u_f)$.

It should also be mentioned that the electronic heat capacitance of bulk silicon has been extracted from low temperature measurements of thermal capacitance by Kobayashi et al [20] for various doping levels and can be well fitted by Eqs (10) or (22) without any parameter adjustment as can be seen from Figure 6, thereby validating our reformulation of C_e.

Therefore, both Figures 3, 4 and 5 indicate that Eqs (19), (20), (21) and (22) do constitute simple and analytical closed-form expressions for calculating the carrier concentration, the electronic thermopower, the reduced electronic heat conductivity and the reduced electronic heat capacitance in silicon as a function of reduced Fermi level from semiconductor regime (Maxwell-Boltzmann statistics) up to metallic regime (degenerate statistics) with a good accuracy for practical use in device numerical simulation.

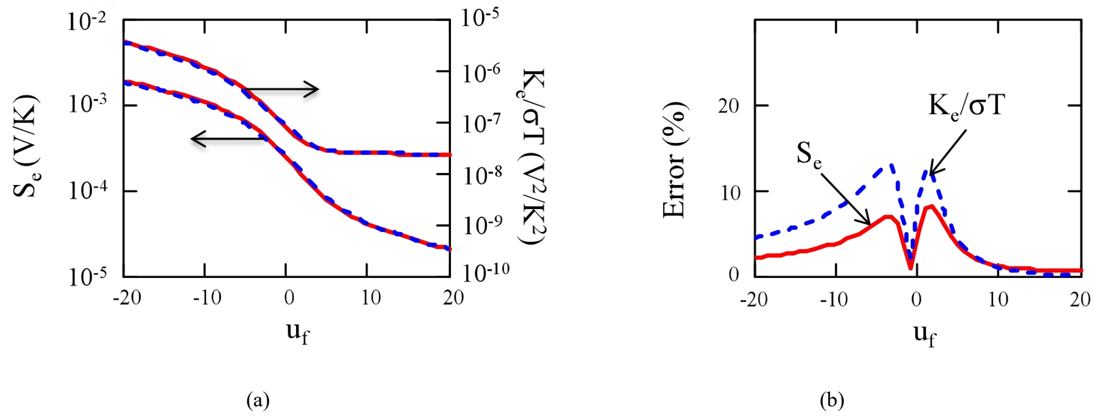

(a) (b)

Figure 4. (a) Variations of electronic thermopower S_e and and reduced electronic heat conductivity $K_e/\sigma T$ with reduced Fermi energy u_f as obtained by exact Fermi-Dirac statistics (solid lines) and by analytical approximation of Eqs (20) and (21) (dahsed lines) and (b) Variations of corresponding error.

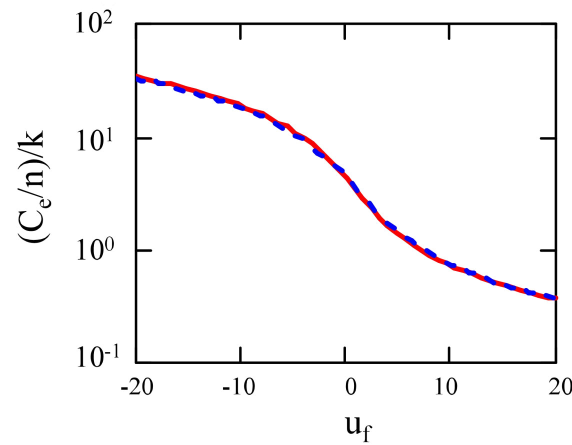

Figure 5. Variations of reduced electronic heat capacitance C_e/n with reduced Fermi energy u_f as obtained by exact Fermi-Dirac statistics (solid lines) and by analytical approximation of Eqs (22) (dahsed lines).

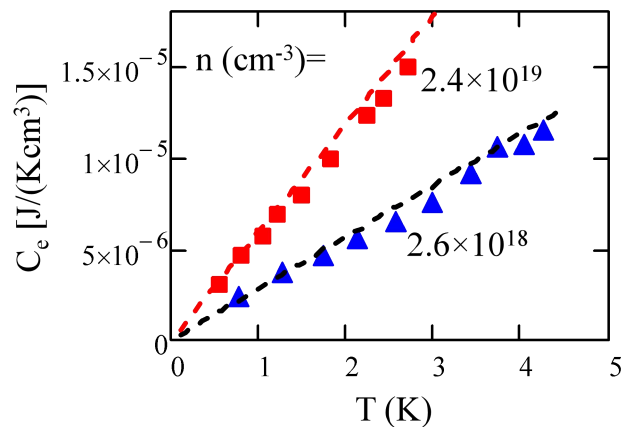

Figure 6. Experimental (symbols) and theoretical (dashed lines) variations of electronic heat capacitance C_e with temperature. Experimental data obtained from Ref. [20] on bulk silicon with various doping levels. Theoretical data from Eqs (10) or (22).

2.2 *Phononic-Related Parameters*

As for C_e, the phonon heat capacitance in a crystal can be evaluated from $C_{ph} = \partial U_{ph} / \partial T$, U_{ph} being the lattice vibrations (phonon) energy and can be equated to as [19],

$$C_{ph} = \frac{\partial U_{ph}}{\partial T} = \frac{\partial \int_0^{+\infty} E \cdot g(E) \cdot f_b \, dE}{\partial T} = \int_0^{+\infty} E \cdot g(E) \cdot \left(\frac{\partial f_b}{\partial T} \right) dE \quad (23)$$

where $f_b(E,T) = 1/\left(e^{E/kT} - 1\right)$ is the Bose-Einstein distribution function and $g(E) \sim E^2$ the phonon density of states at low energies (i.e. for the acoustic branches). This readily yields the so-called Debye formula [19],

$$C_{ph}(T) = 9 \cdot k \cdot N \cdot \left(\frac{T}{T_d} \right)^3 \int_0^{T_d/T} \frac{x^4 e^x}{\left(e^x - 1\right)^2} dx \quad (24)$$

where N is the atom density (=5×10^{22}/cm^3 for silicon) and T_d is the Debye temperature (T_d = 645K for silicon). At high temperature ($T \gg T_d$), the phonon heat capacitance tends to a constant $C_{ph} \approx 3 \cdot k \cdot N$, which corresponds to the Dulong and Petit heat capacitance limit. At low temperature ($T \ll T_d$), the integral in Eq. (24) tends to ≈12.π^4/45, such that the phonon heat capacitance C_{ph} reduces to the usual T^3 power law [19],

$$C_{ph}(T) \approx \frac{12 \cdot \pi^4}{5} \cdot k \cdot N \cdot \left(\frac{T}{T_d} \right)^3 \quad (25)$$

As it was done for the electronic heat capacitance, a closed-form analytical expression can be developed for $C_{ph}(T)$ based on the two asymptotic limits at low and high temperature, yielding the simple expression,

$$C_{ph}(T) = \left[\left(\frac{1}{3 \cdot k \cdot N} \right)^a + \left(\frac{1}{\frac{12 \cdot \pi^4}{5} \cdot k \cdot N \cdot \left(\frac{T}{T_d} \right)^3} \right)^a \right]^{-\frac{1}{a}} \quad \text{with } a \approx 0.85 \quad (26)$$

Figure 7a shows the variations with temperature of the phonon heat capacitance C_{ph} as given by the exact Debye model of Eq. (24) and the simple analytical expression of Eq. (26). As can be seen from the figure, Eq. (26) provides a very good approximation to the exact formula with an error less than ≈12% over the whole temperature range up T_d.

Figure 7b compares the variation with temperature of the phonon heat capacitance as obtained from the Debye model (Eqs 24 or 26) to bulk silicon experimental data from Ref. [21]. It indicates that the Debye model provides a sufficiently good description of the phonon heat capacitance over a wide range of temperature needed for device simulation.

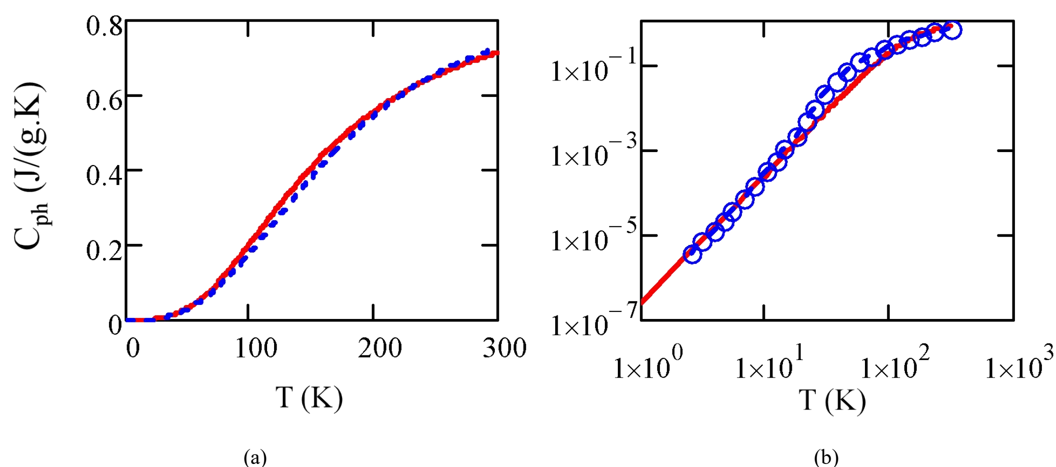

Figure 7. (a) Variations of phonon heat capacitance C_{ph} with temperature as obtained from exact Debye equation (24) (solid line) and analytical approximation formula (26) (dashed line). (b) Experimental (symbols) and theoretical (solid line) variations of phonon heat capacitance C_{ph} with temperature as obtained from bulk silicon data of Ref. [21] and from Debye model of Eqs (24) or (26).

The lattice thermal conduction is governed by the heat transport by phonon diffusion due to a temperature gradient such as the heat flux $J_Q = D_{ph} \cdot dQ/dx = D_{ph}(dQ/dT)\cdot(dT/dx)$, with $D_{ph} = v_s \cdot \lambda_{ph}/3$ being the phonon diffusion coefficient, v_s the phonon sound velocity and λ_{ph} the phonon mean free path. Integrating over all phonon energies for the acoustic branches yields for the phonon heat conductivity $K_{ph} = J_Q/(dT/dx)$ [22,23],

$$K_{ph}(T) = 3 \cdot k \cdot N \cdot \left(\frac{T}{T_d}\right)^3 \int_0^{T_d/T} v_s^{\,2} \cdot \tau_{ph} \cdot \frac{x^4 e^x}{\left(e^x - 1\right)^2} dx \tag{27}$$

where $\tau_{ph} = \lambda_{ph}/v_s$ is the phonon relaxation time, which is in general a function of temperature and phonon energy. If we consider, in first approximation, that τ_{ph} is independent of energy, we can factorize the product $v_s^{\,2}\tau_{ph}$ outside the integral, such that the phonon heat conductivity can be related to the phonon heat capacitance according to the kinetic theory as [24],

$$K_{ph}(T) = \frac{1}{3} C_{ph}(T) \cdot v_s^{\,2} \cdot \tau_{ph} \tag{28}$$

Figure 8 shows how Eq. (28) can be used to fit reasonably well the bulk silicon data from Ref. [23] for $K_{ph}(T)$, provided that the phonon relaxation time is made explicitly temperature dependent as $\tau_{ph} = \tau_{ph0}/\left[1+(T/T_0)^4\right]$. However, in section 3, a more accurate empirical combined power law vs T will be used to fit the $K_{ph}(T)$ silicon data for device simulation purpose (see Eq (42)).

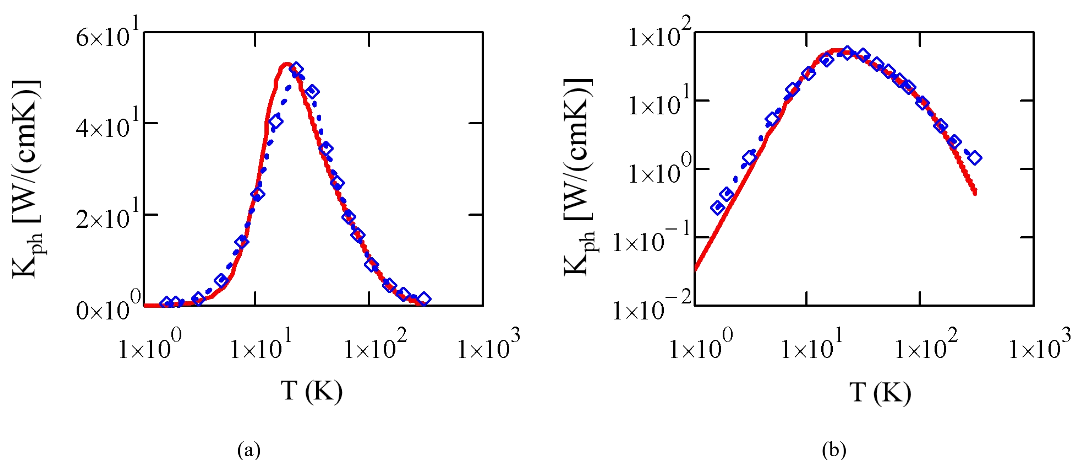

Figure 8. Variations of phonon heat conductivity K_{ph} with temperature T in linear scale (a) and log scale (b) as obtained from Eq. (28) and experimental data of Ref. [23] for bulk silicon (Parameters: $v_s = 9\times10^5$cm/s, $\tau_{ph0} = 0.21$µs and $T_0 = 14$K).

Another important phenomenon appearing at low temperature is the so-called phonon drag effect, which enhances the electronic thermopower due to the interaction between diffusing phonons and electrons. The phonon drag effect has been addressed both experimentally and theoretically in the 50's by Geballe and Hull [25] and Herring [26], whereas further developments have been proposed later by Cantrell and Butcher [27] and Mahan [28]. In first instance, the Herring formula should be used to depict the phonon drag thermopower S_{ph} and can be formulated using the Matthiessen rule as [26],

$$S_{ph}(T) = \frac{v_s^{\,2} \cdot \tau_{ph}(T)}{T \cdot \mu_{eff}(T)} \cdot \frac{\mu_{eff}(T)}{\mu_{effph}(T)} = \frac{v_s^{\,2} \cdot \tau_{ph}(T)}{T \cdot \mu_{effph}(T)} \tag{29}$$

where $\mu_{eff} = \sigma/(q \cdot n)$ is the effective mobility and $\mu_{effph}(T)$ is the phonon-limited electron mobility component described by $\mu_{effph}(T) = 1400 \cdot (T/300)^{-1.5}$ for bulk silicon [29]. As can be seen from Figure 9, Eq. (29) well reproduces the modelling results of Mahan [28], which have been calibrated on Geballe and Hull silicon

experimental data [25] after having adjusted the temperature dependence of the phonon drag relaxation time such as $\tau_{ph} = \tau_{ph0} / \left[1+(T/T_0)^3\right]$. Note that this phonon relaxation time is 2 orders of magnitude lower than the τ_{ph} entering the phonon heat conductivity formula (28). This discrepancy has been discussed in the literature and could be attributed to the difference of nature between pure phonon transport and electron-phonon interaction processes [26–28]. However, it should be mentioned that it is close to the one used in Mahan et al [28] and has the same trend versus T, indicating that Eq. (29) is physically sound. In any case, this is not so important since it is calibrated on both experimental and theoretical silicon data and therefore can be used in first approximation to evaluate the phonon drag thermopower in bulk silicon.

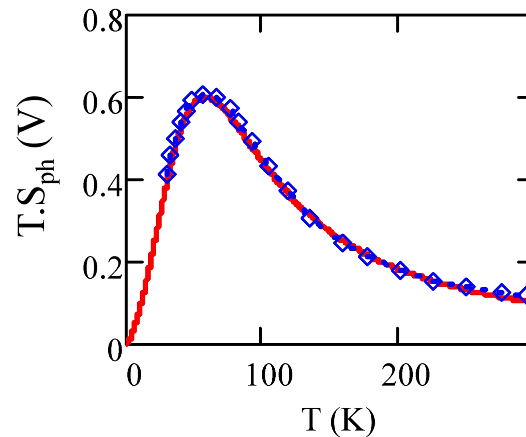

Figure 9. Variations of temperature-phonon drag thermopower product $T{\cdot}S_{ph}$ with temperature T as obtained from model of Eq. (29) and from modelling data of Ref. [28] for bulk silicon (Parameters: $v_s = 9{\times}10^5$cm/s, $\tau_{ph0} = 25$ns and $T_0 = 58$K, Si doping level 10^{15}/cm^3).

Nevertheless, Eq. (29) giving the phonon drag thermopower can be considered as too simplistic to be applied at low temperature where degeneracy occurs. This is why further improvement to (29) has been proposed by Cantrell and Butcher [27] to account for the electron energy dispersion in 2D inversion layers [30]. Applying their derivation to 3D electron gas leads to the generalized expression,

$$S_{ph}(E_f,T) = \frac{v_s^2 \cdot \tau_{ph}(T)}{T \cdot \mu_{eff}(T)} \cdot \frac{\int_0^{+\infty} E \cdot N(E) \cdot \frac{\mu(E,T)}{\mu_{ph}(E,T)} \cdot \left(-\frac{\partial f}{\partial E}\right) dE}{\int_0^{+\infty} E \cdot N(E) \cdot \left(-\frac{\partial f}{\partial E}\right) dE} \tag{30}$$

where the energy mobility functions $\mu(E,T)$ and $\mu_{ph}(E,T)$ are given by,

$$\mu(E,T) = \left[\frac{1}{\mu_{ph}(E,T)} + \frac{1}{\mu_I(E)}\right]^{-1} \tag{31}$$

In Eq. (31), $\mu_{ph}(E,T)$ is the phonon limited mobility function given by [29],

$$\mu_{ph}(E,T) = 1300 \cdot \frac{300}{T} \cdot \left(\frac{E}{E_0}\right)^{-\frac{1}{2}} \quad (\text{cm}^2/\text{Vs}) \tag{32a}$$

and $\mu_I(E)$ is the ionized and neutral imputity limited mobility function which can be expressed as [29],

$$\mu_I(E,T) = 600 \cdot \frac{N_{d0}}{N_d} \cdot \left(\frac{E}{E_0}\right)^{\frac{3}{2}} + 80 \quad (\text{cm}^2/\text{Vs}) \tag{32b}$$

where N_d is the silicon doping concentration, $N_{d0} = 2.5 \cdot 10^{17}/\text{cm}^3$ and $E_0 = 50\text{meV}$.

Note that the parameters used in Eq. (32) have been properly calibrated such that the effective mobility $\mu_{eff} = \sigma/(q \cdot n)$ calculated with Eqs (1), (3), (31) and (32) fits reasonably well the standard electron mobility data versus doping level at room temperature for silicon [31] as shown in Figure 10.

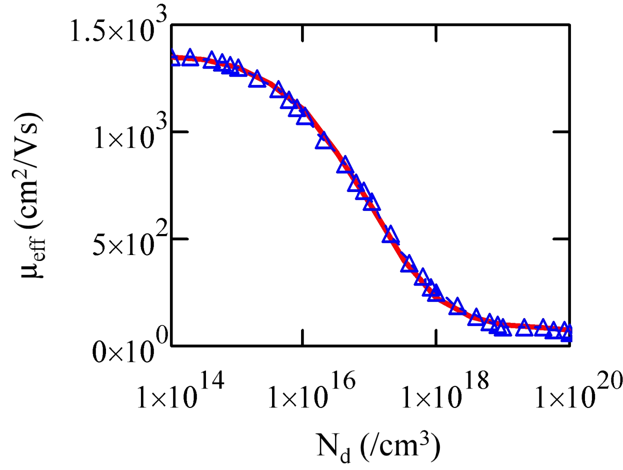

Figure 10. Variations of electron effective mobility μ_{eff} with doping level N_d as obtained from modelling with Eqs (1), (3), (31) and (32) (red solid line) and from experiment (room temperature standard Si data [31]).

Besides, it is worthwhile to examine which are the asymptotic limits of the Cantrell and Butcher equation (30) for Maxwell-Boltzmann and degenerate metallic statistics. In the case of MB statistics, Eq (30) can be well approximated by,

$$S_{ph}(T) = \frac{v_s^2 \cdot \tau_{ph}(T)}{T \cdot \mu_{ph}(3kT)} \tag{33}$$

which is nothing else than Herring's formula (29).

In the case of degenerate statistics, Eq. (30) reduces to,

$$S_{ph}(E_f, T) = \frac{v_s^2 \cdot \tau_{ph}(T)}{T \cdot \mu_{ph}(E_f, T)} \tag{34}$$

indicating that S_{ph} now depends directly on the phonon limited mobility function at Fermi energy $\mu_{ph}(E_f, T)$.

Figure 11a shows the variations of the phonon drag thermopower S_{ph} with temperature as obtained from Cantrell and Butcher model [27] of Eq. (30) and corresponding MB and degenerate approximations given by Eqs (33) and (34), respectively. We can notice that, for such doping level (here $N_d = 3\times10^{17}/\text{cm}^3$), the degeneracy prevails only below $T \approx 5\text{K}$, whereas MB statistics dominates for all higher temperatures. Figure 11b reveals that, for low doping level (here $N_d = 10^{15}/\text{cm}^3$), the Cantrell and Butcher model [27] of Eq. (30) provides similar results than Mahan modelling data [28] calibrated on Geballe and Hull [25] experiments. Therefore, it appears clearly that Eq. (30) allow to extend the range of application of the Herring formula (29) to the degenerate case at very low temperature and/or higher doping level.

These results also reveal that, for low doped silicon used in FDSOI MOS channel, the Herring formula of Eq. (29) calibrated on Mahan modelling results and Geballe and Hull experimental silicon data should constitute a first approximation for the phonon drag thermopower evaluation. Nevertheless, it should be mentioned that it is not able to describe the temperature and 2D carrier density dependence obtained at very low temperature in MOS inversion layers by Gallagher et al [32]. This issue goes beyond the scope of the present theoretical analysis and should be further discussed.

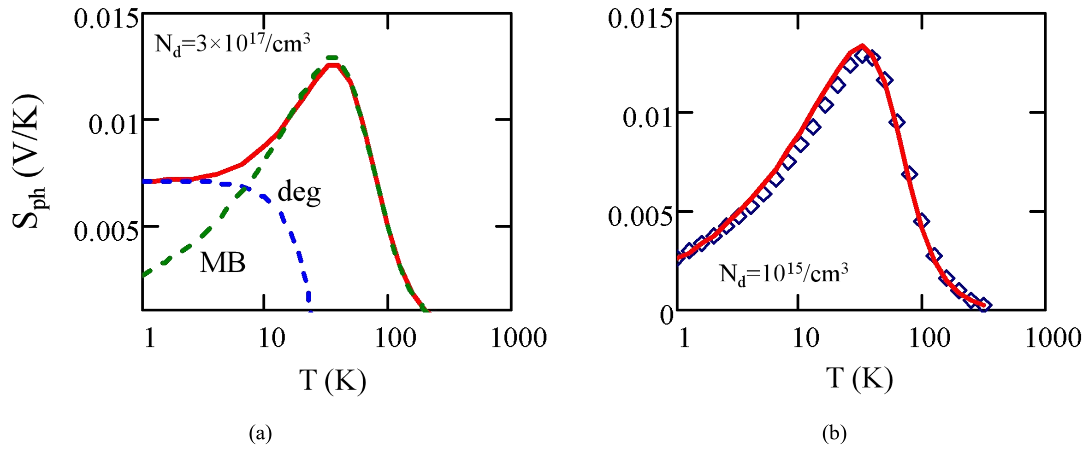

Figure 11. Variations of phonon drag thermopower S_{ph} with temperature T: (a) as obtained from Cantrell and Butcher model [27] of Eq. (30) (red solid line) and from MB and degenerate asymptotic approximations (dashed lines) of Eqs (33) and (34), and, (b) as obtained from Eq. (30) (solid line) and extrapolated Mahan's data [28] (symbols) for low doped silicon (Parameters: v_s = 9×10^{5}cm/s, τ_{ph0} = 18ns and T_0= 58K).

3. Results and Discussion

The electro-thermal properties of a FDSOI MOS structure have been simulated after solving the Poisson equation in two dimensions using the finite element partial differential equation software FlexPDE [33]. The simulated SOI structure is illustrated in Figure 12 and features a 2nm EOT (equivalent oxide thickness) top oxide thickness, a 10nm undoped silicon film and a 20nm buried oxide (BOX). No source and drain electrodes were considered here since limiting our analysis to 1D profiles, sufficient to evaluate in a long channel the sheet quantities integrated over the silicon thickness. For simplicity, the front (resp. back) gate voltage V_{g1} (resp. V_{g2}) was directly applied to the top (resp. bottom) oxide external boundary. In this case, the electrical potential V across the structure follows the Poisson equation as,

$$\nabla(\varepsilon_{si}\nabla V) = q\cdot\left[n\left(\frac{q(V-V_0)}{kT}\right) - p\left(\frac{q(-V-V_0)}{kT}\right)\right] \quad \text{(Silicon)} \tag{35a}$$

$$\nabla(\varepsilon_{ox}\nabla V) = 0 \quad \text{(Oxide)} \tag{35b}$$

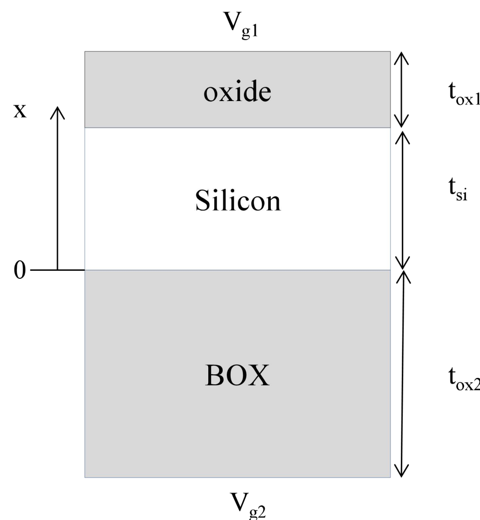

Figure 12. Schematic of FDSOI structure used for simulation (t_{ox1} = 2nm, t_{ox2} = 20nm, t_{si} = 10nm).

where ε_{ox} and ε_{si} being the oxide and silicon permittivities, respectively, and V_0 (≈0.55V) the mid-gap potential. The carrier concentrations in Eq. (35a) were computed using the analytical approximation of Eq. (19). Quantum confinement effects were taken into account using Hansch's quantum correction at each Si-SiO_2 interface with a

quantum length of 1nm as in [14]. Once the electron density $n(x)$ was known from Poisson's equation solution, the electronic thermopower S_e, the reduced electronic heat conductivity $K_e/(\sigma T)$ and the reduced electronic heat capacitance C_e/n across the silicon film were then calculated using Eqs (20), (21) and (22).

In Figure 13 are illustrated typical spatial variations of the electron density $n(x)$ across the silicon channel for a FDSOI MOSFET biased in strong inversion ($V_{g1}=1.5\text{V}$, $V_{g2}=0$) and for various temperatures varying from 300K down to 1K. From the log scale plot of this figure, one can clearly see the progressive depopulation of the carriers from the BOX interface (left side) as the temperature is lowered. Instead, the linear scale plot indicates that the carrier profiles near the top oxide interface (right side) are nearly temperature independent since the device is polarized in strong inversion.

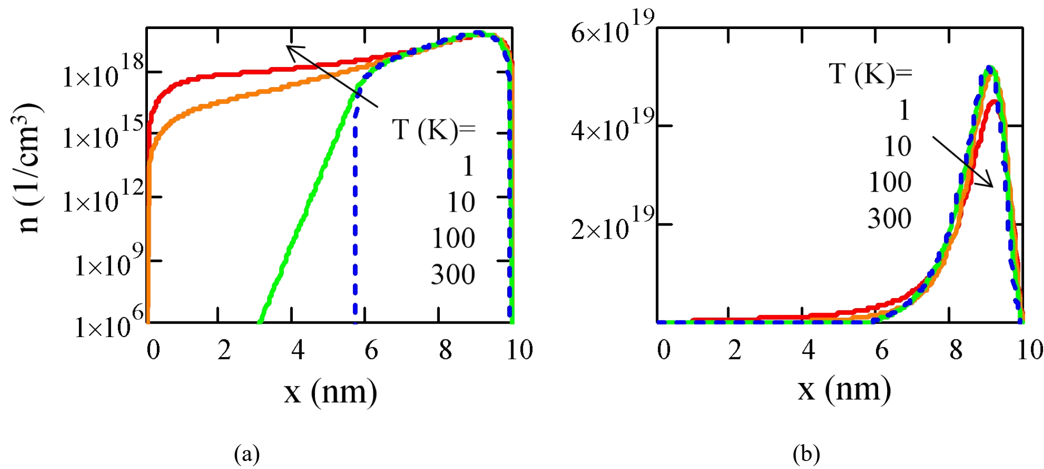

Figure 13. Spatial variations of the electron density $n(x)$ plotted in log scale (a) and linear scale (b) for various temperatures as obtained in a FDSOI structure biased in strong inversion (t_{ox1} = 2nm, t_{ox2} = 20nm, t_{si} = 10nm, V_{g1}=1.5V, V_{g2}=0).

Figure 14 shows the corresponding spatial variations of the normalized electronic thermopower $S_e/T(x)$ and of the reduced electronic heat conductivity $K_e/(\sigma T)(x)$ across the silicon film calculated with Eqs (20) and (21). As was explained in Figure 2, both the electronic thermopower and reduced electronic heat conductivity increase as the carrier concentration diminishes within Maxwell-Boltzmann statistics, whereas the normalized electronic thermopower S_e/T and the reduced electronic heat conductivity $K_e/(\sigma T)$ reach their temperature independent degenerate limits at high carrier concentration and/or at very low temperature. Since C_e/n is proportional to S_e (see Eq. (22)) it presents the same spatial variations than S_e (not shown).

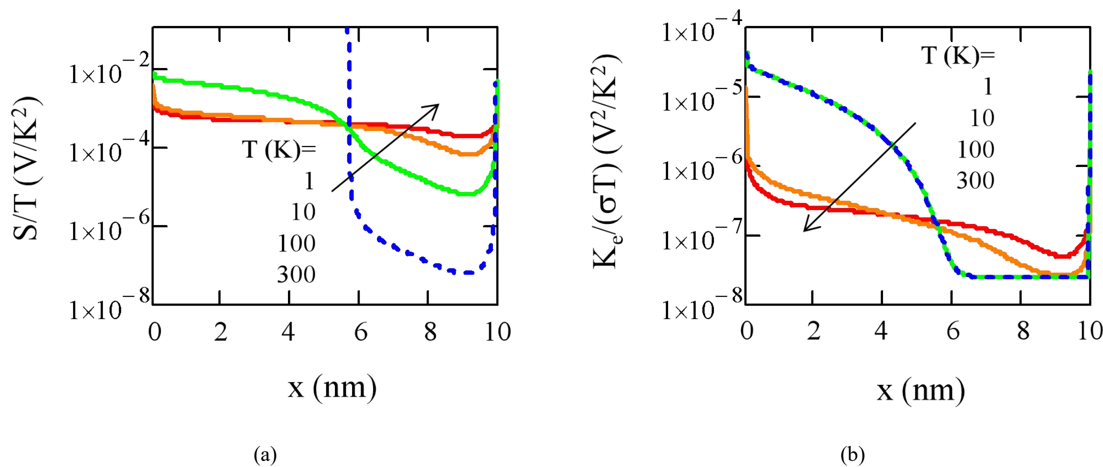

Figure 14. Spatial variations of the electronic thermopower $S_e(x)$ (a) and of the reduced electronic heat conductivity $K_e/(\sigma T)(x)$ (b) for various temperatures as obtained in a FDSOI structure biased in strong inversion (t_{ox1} = 2nm, t_{ox2} = 20nm, t_{si} = 10nm, V_{g1}=1.5V, V_{g2}=0).

The sheet carrier density N_s was then calculated by integrating the electron concentration $n(x)$ across the silicon channel as,

$$N_s = \int_0^{t_{si}} n(x)\,dx \tag{36}$$

Typical variations of the inversion charge density N_s with front gate voltage V_{g1} are shown in Figure 15 for various temperatures both in log and linear scales. One should clearly notice the usual strong increase of the subthreshold slope as the temperature is lowered due to the onset of Maxwell-Boltzmann statistics [1,2]. In contrast, at strong inversion above threshold, as is well known [1,2], the sheet carrier density N_s becomes nearly temperature independent.

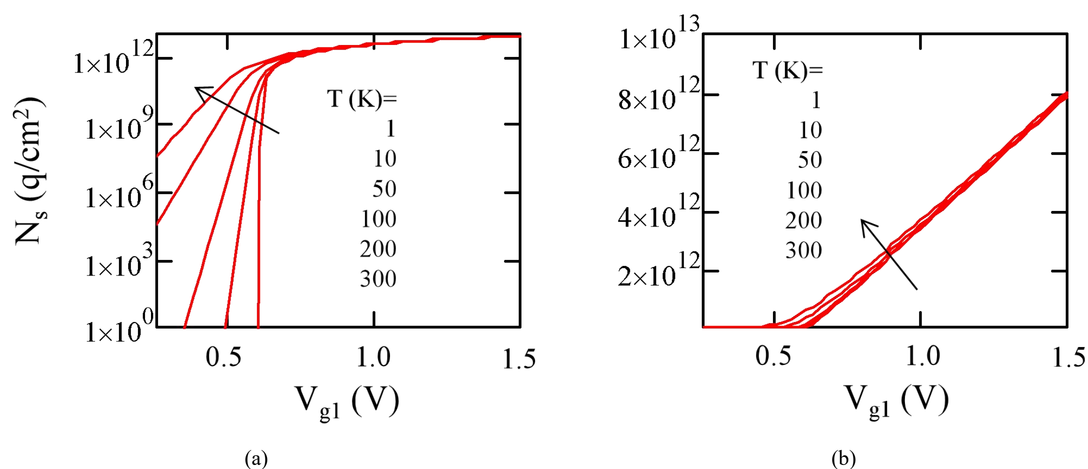

Figure 15. Variations with front gate voltage V_{g1} of the sheet carrier density N_s in log scale (a) and linear scale (b) for various temperatures as obtained in a FDSOI structure (t_{ox1} = 2nm, t_{ox2} = 20nm, t_{si} = 10nm, V_{g2}=0).

The local electrical conductivity $\sigma(x)$ was then evaluated by considering a standard mobility law both depending on temperature and local vertical electric field F_x as [14,34],

$$\sigma(x,T) = q \cdot \mu(x,T) \cdot n(x) \tag{37a}$$

$$\text{with } \mu_0(T) = \left[\frac{1}{3000} + \frac{1}{600}\left(\frac{T}{300}\right)\right]^{-1} \text{(cm}^2\text{/Vs)} \tag{37b}$$

$$\text{and } \mu(x,T) = \frac{\mu_0(T)}{1+\left(\dfrac{F_x}{F_c}\right)^2} \tag{37c}$$

where F_c is a critical field (≈1MV/cm) allowing to emulate the mobility degradation at high gate voltage due to the surface roughness scattering. The low field empirical mobility law $\mu_0(T)$ accounts for the mobility increase with temperature reduction governed by phonon scattering and for mobility saturation at low temperature due to prevailing neutral defect scattering [2,35]. Knowing the local electrical conductivity $\sigma(x)$, it is then possible to calculate the sheet electrical conductivity σ_s by integrating the parallel contribution to charge transport of each channel layer as,

$$\sigma_s = \int_0^{t_{si}} \sigma(x,T)\,dx \tag{38}$$

In Figure 16 are reported typical evolutions of the sheet electrical conductivity σ_s with front gate voltage V_{g1} for various temperatures from 300K down to 1K, as obtained from Eqs (37) and (38). As for the $N_s(V_{g1})$ characteristics, one should also note the strong increase of the subthreshold slope with temperature lowering when Maxwell-Boltzmann's statistics prevails. However, in this case, the sheet electrical conductivity σ_s is

significantly improved above threshold at low temperature due to the low field mobility enhancement. The onset of a zero temperature coefficient point (ZTC) in the $\sigma_s(V_{g1})$ is noticeable and is the consequence of the ≈1/T mobility dependence. It should be pointed out that this is in full agreement with usual cryogenic transfer characteristics data obtained in long channel Si MOSFETs [2,35]. It should also be mentioned that the effective mobility deduced from the sheet conductivity $\mu_{eff} = \sigma_s / (qN_s)$ exhibits variation with temperature from 400 cm^2/Vs at 300K up to 2500 cm^2/Vs at 10K (not shown here), which are in good agreement with the experimental data obtained on FDSOI MOSFETs [35,36].

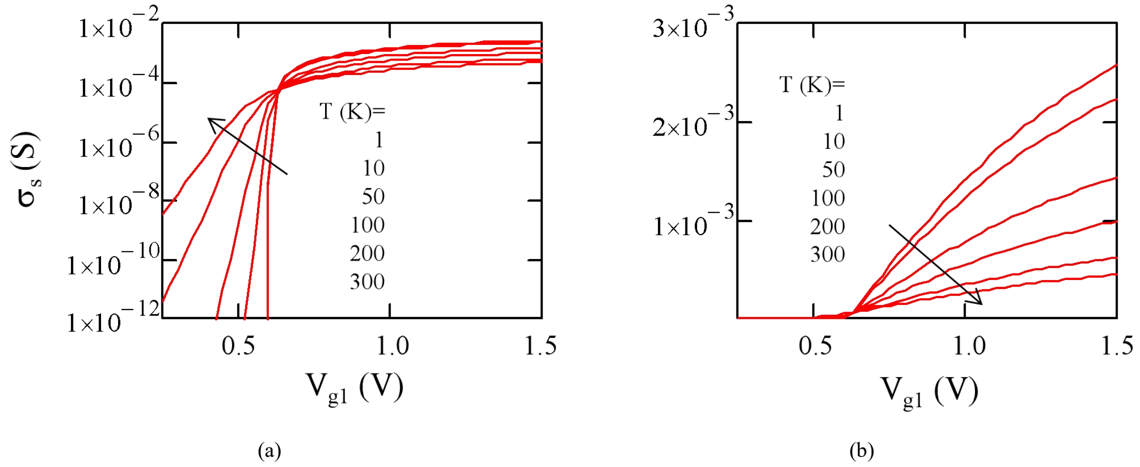

Figure 16. Variations with front gate voltage V_{g1} of the sheet electrical conductivity σ_s in log scale (left) and linear scale (right) for various temperatures as obtained in a FDSOI structure (t_{ox1} = 2nm, t_{ox2} = 20nm, t_{si} = 10nm, V_{g2}=0).

Once having evaluated the local and sheet electrical conductivity, it is now possible to calculate the sheet electronic thermopower S_{es}, the sheet electronic heat conductivity K_{es} and the sheet electronic heat capacitance C_{es} by integrating the parallel contribution of each channel layer to electronic and heat transport as [18,37],

$$S_{es} = \frac{\int_0^{t_{si}} \sigma(x,T) \cdot S(x,T)\, dx}{\int_0^{t_{si}} \sigma(x,T)\, dx} \quad (39)$$

$$\frac{K_{es}}{\sigma_s T} = \frac{\int_0^{t_{si}} K_e(x,T)\, dx}{T \cdot \int_0^{t_{si}} \sigma(x,T)\, dx} \quad (40)$$

and

$$\frac{C_{es}}{N_s} = \frac{\int_0^{t_{si}} C_e(x,T)\, dx}{\int_0^{t_{si}} n(x)\, dx} \quad (41)$$

Representative variations of the sheet thermopower S_{es} and reduced sheet electronic heat conductivity $K_{es} / (\sigma_s T)$ with front gate voltage V_{g1} are depicted in Figure 17 for various temperatures from 300K down to 1K as obtained using Eqs (39) and (40). Overall, S_{es} and $K_{es} / (\sigma_s T)$ diminish as the temperature is increasing, which is mainly due to the augmentation of the sheet carrier concentration with front gate voltage. Below threshold, both S_{es} and $K_{es} / (\sigma_s T)$ sharply increase as the temperature is lowered due the onset of subthreshold regime. Since the variations of C_{es} / N_s with V_{g1} and temperature resemble those of $S_{es} / (V_{g1}, T)$, they are not shown here.

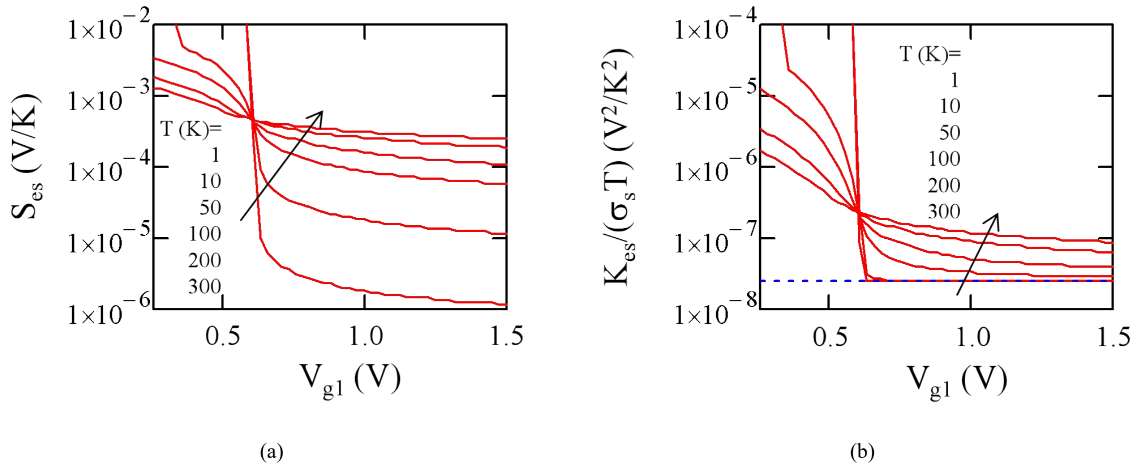

(a) (b)

Figure 17. Variations with front gate voltage V_{g1} of the sheet thermopower S_{es} and reduced sheet electronic heat conductivity $K_{es}/(\sigma_s T)$ for various temperatures as obtained in a FDSOI structure (t_{ox1} = 2nm, t_{ox2} = 20nm, t_{si} = 10nm, V_{g2}=0).

Moreover, the other electro-thermal parameters of interest for semiconductor devices related to S_{es} and K_{es} are the Peltier coefficient, $Pel = T \cdot S_{es}$, and thermoelectric figure-of-merit factor $zT = \sigma_s \cdot T \cdot S_s^{\,2} / K_{ths}$, K_{ths} being the whole sheet thermal conductivity of the silicon channel. The latter can be obtained by adding the sheet electronic heat conductivity K_{es} to the channel sheet phonon heat conductivity $K_{phs} = K_{ph} \cdot t_{si}$, where K_{ph} is the phonon heat conductivity of undoped bulk silicon, so that $K_{ths} = K_{es} + K_{phs}$. Instead of using Eq. (28) of section 2 for $K_{ph}(T)$, the bulk silicon heat conductivity data from Callaway [22] were adapted to account for the reduction of K_{ph} in thin silicon film (here 10nm) due to increased phonon boundary scattering using the approach of Ashegi et al [38] and were interpolated versus temperature by a combined power law analytical function of the form,

$$K_{ph}(T) = (13 \cdot T^{-2.5} + 1.2\times10^{-4} \cdot T)^{-1} \ \left[\mathrm{W/(cm \cdot K)}\right] \tag{42}$$

It should be mentioned that the thermal leakage in the front and BOX oxides surrounding the channel have been overlooked since their heat conductivity is at least two orders of magnitude lower than those of bulk silicon.

In Figure 18a are compared the variations with temperature of the total sheet thermal conductivity K_{tots} with the electronic (K_{es}) and phonon (K_{phs}) components as obtained using Eqs (40) and (42) for a FDSOI MOSFET biased in strong inversion ($V_{g1} = 1.5\mathrm{V}$). This figure clearly reveals that the phonon contribution dominates the channel thermal conduction down to very low temperature (≈3K), whereas the channel electronic heat conductivity K_{es} only prevails at extreme low temperature below ≈0.3K. Similarly, in Figure 18b are displayed the variations with temperature of the total sheet thermal capacitance C_{tots} (=C_{es}+C_{phs}) with the electronic (C_{es}) and phonon ($C_{phs} = C_{ph} \cdot t_{si}$) components as obtained using Eqs (41) and (26) for a FDSOI MOSFET biased in strong inversion ($V_{g1} = 1.5\mathrm{V}$). The figure also clearly indicates that the phonon contribution C_{phs} to the total sheet thermal capacitance dominates above ≈6K, whereas the electronic contribution C_{es} prevails at very low temperature below ≈1K.

Moreover, the combination of the sheet thermal capacitance and sheet thermal channel resistance, defined as $R_{ths} = L / K_{tots}$, allows us to evaluate the channel total thermal response time $\tau_{tot} = R_{ths} \cdot C_{tots} \cdot L / 6 (= C_{tots} \cdot L^2 / (6K_{tots}))$, L being the channel length, in analogy to what is done for the channel electronic response time [39]. Figure 19 shows the variations with temperature of the total channel thermal response time τ_{tot} along with its phonon $\tau_{ph} (= C_{phs} \cdot L^2 / (6K_{phs}))$ and electronic $\tau_e (= C_{es} \cdot L^2 / (6K_{es}))$ components as obtained for a FDSOI MOSFET biased in strong inversion ($V_{g1} = 1.5\mathrm{V}$) with a channel length $L = 100\mathrm{nm}$. As can be seen from the figure, the thermal response time is dominated by the phonon contribution above ≈10K, while it is mainly controlled by the electronic contribution below ≈1K. Note that for such a gate length, the channel thermal response time lies in the picosecond range below 10K.

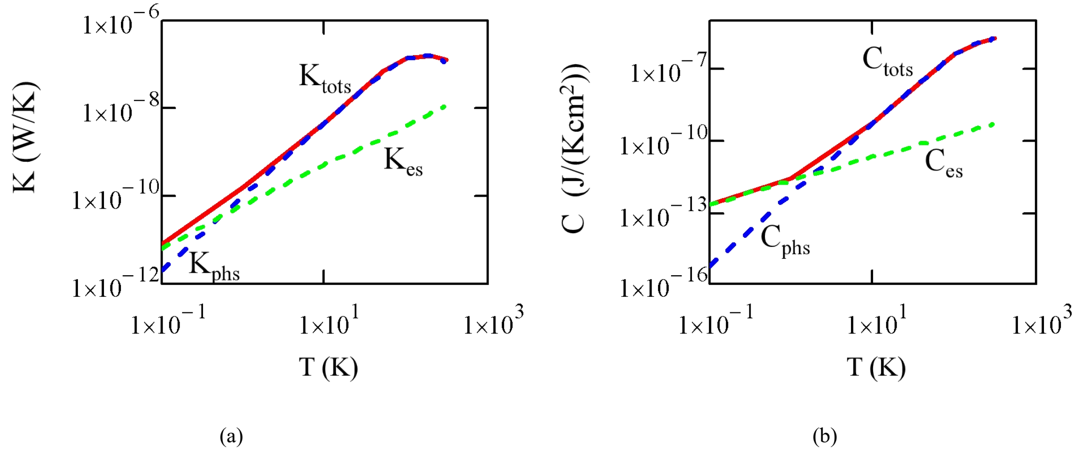

Figure 18. (a) Variations with temperature of whole sheet thermal conductivity K_{tots} (red solid line), sheet phonon thermal conductivity K_{phs} (blue dashed line) and sheet electronic thermal conductivity K_{es} (green dashed line). (b) Variations with temperature of whole thermal capacitance C_{tots} (red solid line), sheet phonon thermal capacitance C_{phs} (blue dashed line) and sheet electronic thermal capacitance C_{es} (green dashed line) as obtained in a FDSOI structure (t_{ox1} = 2nm, t_{ox2} = 20nm, t_{si} = 10nm, V_{g1}=1.5V, V_{g2}=0).

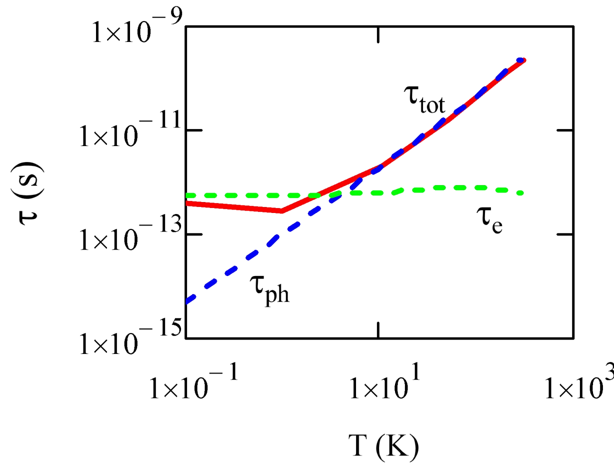

Figure 19. Variations with temperature of the total thermal response time τ_{tot} (red solid line), thermal phonon response time τ_{ph} (blue dashed line) and electronic response time τ_e (green dashed line) as obtained in a FDSOI structure (t_{ox1} = 2nm, t_{ox2} = 20nm, t_{si} = 10nm, L = 100nm, V_{g1}=1.5V, V_{g2}=0).

The variations of the Peltier coefficient Pel and thermoelectric figure-of-merit factor zT with front gate voltage V_{g1} can be evaluated as shown in Figure 20. As can be seen, the Peltier coefficient variations with gate voltage mainly mimic those of the thermopower above threshold, whereas there is a relative temperature independency below threshold. Similarly, the thermoelectric figure-of-merit factor variations with gate voltage are mainly controlled by those of the electrical conductivity below threshold, whereas they are mostly reflecting those of $\sigma_s \cdot S_{es}{}^2$ in strong inversion, since K_{ths} is constant with V_{g1} as being mostly dominated by the sheet phonon heat conductivity term (see Figure 18). In any case, both the Peltier coefficient and the thermoelectric figure-of-merit factor take values well below one, indicating a poor thermoelectric efficiency for such a FDSOI MOSFET, especially at cryogenic temperatures, indicating that such structures are not optimized for pure thermoelectric applications.

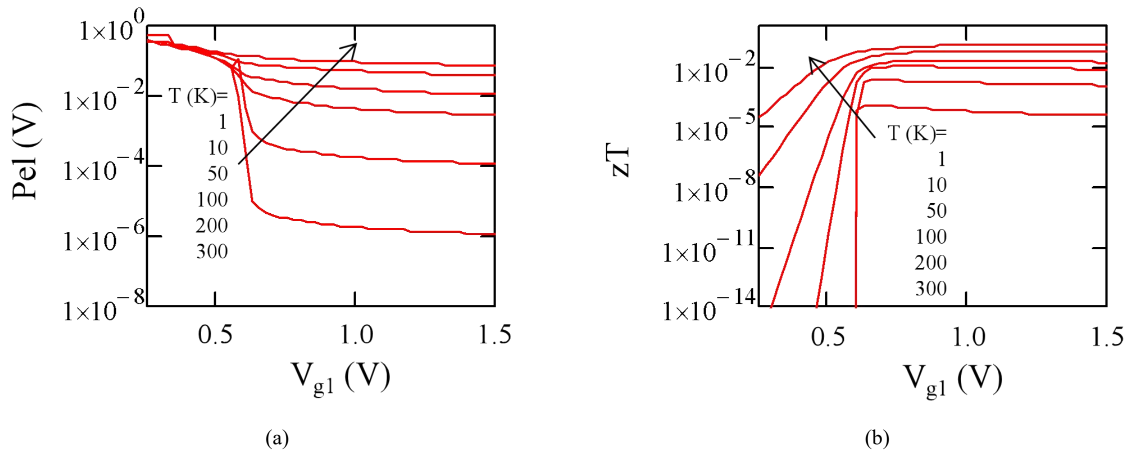

Figure 20. Variations with front gate voltage V_{g1} of the Peltier coefficient *Pel* and thermoelectric figure of merit factor *zT* for various temperatures as obtained in a FDSOI structure (t_{ox1} = 2nm, t_{ox2} = 20nm, t_{si} = 10nm, V_{g1}=1.5V, V_{g2}=0).

Finally, in Figure 21 are compared, for completeness, the variations with temperature of the sheet electronic thermopower S_{es} for two front gate voltages V_{g1} and of the phonon drag thermopower S_{ph} as given by the extrapolated Mahan model [28] of Eq. (29) calibrated on Geballe and Hull silicon data [25]. It appears from the figure that the phonon drag thermopower component should dominate the electronic thermopower component, especially below T≈50K (see Figure 11). However, these results have to be taken with caution since the simple model of Eq. (29) does not account for the $1/n$ and T^3 dependence of the thermopower observed at very low temperature e.g. by Gallagher et al in Si MOS inversion layers [32]. Therefore, a more accurate modelling of the phonon drag thermopower component should be developed, especially at very low temperatures, as a function of carrier concentration (i.e. also Fermi level) and temperature to be further included in FDSOI MOSFET simulation, bringing more reliable electro-thermal simulation results. But this issue goes beyond the scope of this paper.

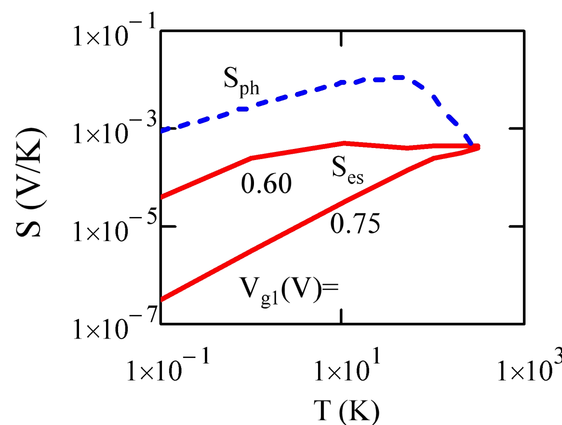

Figure 21. Variations with temperature *T* of the sheet electronic thermopower S_{es} for two front gate voltages V_{g1} (red solid lines) and of the phonon drag thermopower S_{ph} as given by Mahan model [28] of Eq. (29) (blue dashed line) as obtained in a FDSOI structure (t_{ox1} = 2nm, t_{ox2} = 20nm, t_{si} = 10nm, V_{g2}=0).

4. Summary and Conclusions

In this work, we have proposed an original reformulation of the thermopower *S*, heat conductivity *K* and heat capacitance *C* coefficients for electron in bulk silicon as a function of Fermi level position and temperature applicable from Maxwell-Boltzmann to degenerate statistics. Similarly, the phonon related coefficients have also been reformulated in this context. Besides, we have also developed closed-form analytical approximations for these coefficients versus Fermi level, temperature and/or carrier concentration, and which are useful for implementation in TCAD simulation. Then, these analytical expressions for *S*, *K* and *C* have been further

employed to simulate the electro-thermal properties of a FDSOI MOSFET versus front gate voltage from room down to very low temperature (0.1K). The obtained results enable the discrimination between the electron and phonon contributions to the whole properties. These analyses pave the way to further 2D/3D fully coupled electro-thermal numerical simulations of FDSOI MOSFETs down to very deep cryogenic temperatures for full assessment of their electro-thermal performances (transport, self-heating…).

Conflict of Interest

There is no conflict of interest for this study.

References

[1] Gutierrez-D, E.A.; Deen, J.; Claeys, C. *Low temperature electronics: physics, devices, circuits, and applications*. Academic Press: Cambridge, MA, USA, 2001; pp. 1–964.

[2] Balestra, F.; Ghibaudo, G. *Device and circuit cryogenic operation for low temperature electronics.* Springer: New York, NY, USA, 2001; pp. 1–262.

[3] Wada, T.; Nagata, H.; Ikeda, H.; Arai, Y.; Ohno, M.; Nagase, K. Development of Low Power Cryogenic Readout Integrated Circuits Using Fully-Depleted-Silicon-on-Insulator CMOS Technology for Far-Infrared Image Sensors. *J. Low Temp. Phys.* **2012**, *167*, 602–608, https://doi.org/10.1007/s10909-012-0461-6.

[4] Incandela, R.M.; Song, L.; Homulle, H.; Charbon, E.; Vladimirescu, A.; Sebastiano, F. Characterization and Compact Modeling of Nanometer CMOS Transistors at Deep-Cryogenic Temperatures. *IEEE J. Electron Devices Soc.* **2018**, *6*, 996–1006, https://doi.org/10.1109/jeds.2018.2821763.

[5] Charbon, E.; Sebastiano, F.; Vladimirescu, A.; Homulle, H.; Visser, S.; Song, L.; Incandela, R.M. Cryo-CMOS for quantum computing. In Proceedings of 2016 IEEE International Electron Devices Meeting (IEDM), San Francisco, CA, USA, 3–7 December 2016, https://doi.org/10.1109/IEDM.2016.7838410.

[6] Beckers, A.; Jazaeri, F.; Enz, C. Characterization and Modeling of 28-nm Bulk CMOS Technology Down to 4.2 K. *IEEE J. Electron Devices Soc.* **2018**, *6*, 1007–1018, https://doi.org/10.1109/jeds.2018.2817458.

[7] Chakraborty, W.; Aabrar, K. A.; Gomez, J.; Saligram, R.; Raychowdhury, A.; Fay, P.; Datta, S. Characterization and Modeling of 22 nm FDSOI Cryogenic RF CMOS. *IEEE J. Explor. Solid-State Comput. Devices Circuits*, **2021**, *7*, 184–192, https://doi.org/10.1109/JXCDC.2021.3131144.

[8] Pahwa, G.; Kushwaha, P.; Dasgupta, A.; Salahuddin, S.; Hu, C. Compact Modeling of Temperature Effects in FDSOI and FinFET Devices Down to Cryogenic Temperatures. *IEEE Trans. Electron Devices* **2021**, *68*, 4223–4230, https://doi.org/10.1109/ted.2021.3097971.

[9] Bohuslavskyi, H.; Jansen, A.G.M.; Barraud, S.; Barral, V.; Casse, M.; Le Guevel, L.; Jehl, X.; Hutin, L.; Be rtrand, B.; Billiot, G.; et al. Cryogenic Subthreshold Swing Saturation in FD-SOI MOSFETs Described wit h Band Broadening. *IEEE Electron Device Lett.* **2019**, *40*, 784–787, https://doi.org/10.1109/led.2019.29031 11.

[10] Hornibrook, J.M.; Colless, J.I.; Lamb, I.D.C.; Pauka, S.J.; Lu, H.; Gossard, A.C.; Watson, J.D.; Gardner, G.C.; Fallahi, S.; Manfra, M.J.; et al. Cryogenic Control Architecture for Large-Scale Quantum Computing. *Phys. Rev. Appl.* **2015**, *3*, https://doi.org/10.1103/physrevapplied.3.024010.

[11] Maurand, R.; Jehl, X.; Kotekar-Patil, D.; Corna, A.; Bohuslavskyi, H.; Laviéville, R.; Hutin, L.; Barraud, S.; Vinet, M.; Sanquer, M.; et al. A CMOS silicon spin qubit. *Nat. Commun.* **2016**, *7*, 13575. https://doi.org/10. 1038/ncomms13575.

[12] Dhillon, P.; Dao, N.C.; Leong, P.H.; Wong, H.Y. TCAD modeling of cryogenic nMOSFET ON-state current and subthreshold slope. In Proceedings of 2021 International Conference on Simulation of Semiconductor Processes and Devices (SISPAD), Dallas, TX, USA, 27–29 September 2021, https://doi.org/10.1109/SISPAD54002.2021.9592586.

[13] Kriekouki, I.; Beaudoin, F.; Philippopoulos, P.; Zhou, C.; Lemyre, J.C.; Rochette, S.; Mir, S.; Barragan, M. J.; Pioro-Ladrière, M.; Galy, P. Interpretation of 28 nm FD-SOI quantum dot transport data taken at 1.4 K u sing 3D quantum TCAD simulations. *Solid-State Electron.* **2022**, *194*, 108355, https://doi.org/10.1016/j.sse. 2022.108355.

[14] Catapano, E.; Cassé, M.; Gaillard, F.; de Franceschi, S.; Meunier, T.; Vinet, M.; Ghibaudo, G. TCAD simulations of FDSOI devices down to deep cryogenic temperature. *Solid-State Electron.* **2022**, *194*, 108319, https://doi.org/10.1016/j.sse.2022.108319.

[15] Blakemore, J.S. *Semiconductor statistics*. Dover Publication: Mineola, NY, USA, 1987; pp. 1–381.
[16] Mott, N.F.; Davis, E.A. *Electronic Processes in Non-Crystalline Materials*. Oxford University Press: Oxford, UK, 1979; pp. 1–590.
[17] Ghibaudo, G. Transport in the inversion layer of a MOS transistor: use of Kubo-Greenwood formalism. *J. Solid State Phys.* **1986**, *19*, 767, https://doi.org/10.1088/0022-3719/19/5/015.
[18] Lundstrom, M. *Fundamentals of Carrier Transport*. Addison-Wesley: Boston, MA, USA,1990; pp.XX-XX.
[19] Kittel, C. *Introduction to solid state physics*. John Wiley & Sons: New York, NY, USA, 2005; pp. 1–680.
[20] Kobayashi, N.; Ikehata, S.; Sasaki, W. Specific heat study of heavily P doped Si. *Solid State Commun.* **1977**, *24*, 67–70, https://doi.org/10.1016/0038-1098(77)90567-1.
[21] Flubacher, P.; Leadbetter, A.J.; Morrison, J.A. The heat capacity of pure silicon and germanium and propert ies of their vibrational frequency spectra. *Phil. Mag.* **1959**, *4*, 273–294, https://doi.org/10.1080/1478643590 8233340.
[22] Callaway, J. Model for Lattice Thermal Conductivity at Low Temperatures. *Phys. Rev.* **1959**, *113*, 1046–10 51, https://doi.org/10.1103/physrev.113.1046.
[23] Holland, M.G. Analysis of Lattice Thermal Conductivity. *Phys. Rev.* **1963**, *132*, 2461–2471, https://doi.org/ 10.1103/physrev.132.2461.
[24] Ziman, J.M. *Electrons and Phonons*. Oxford University Press: Oxford, UK, 1960; pp. 1–568.
[25] Geballe, T.H.; Hull, G.W. Seebeck Effect in Silicon. *Phys. Rev.* **1955**, *98*, 940–947, https://doi.org/10.1103/ physrev.98.940.
[26] Herring, C. Theory of the Thermoelectric Power of Semiconductors. *Phys. Rev.* **1954**, *96*, 1163–1187, https: //doi.org/10.1103/physrev.96.1163.
[27] Cantrell, D.G.; Butcher, P.N. A calculation of the phonon-drag contribution to the thermopower of quasi-2D electrons coupled to 3D phonons. I. General theory. *J. Phys. C: Solid State Phys*. **1987**, *20*, 1985, https://doi.org/10.1088/0022-3719/20/13/014.
[28] Mahan, G.D.; Lindsay, L.; Broido, D.A. The Seebeck coefficient and phonon drag in silicon. *J. Appl. Phys.* **2014**, *116*, 245102, https://doi.org/10.1063/1.4904925.
[29] Kireev, P. *La physique des semiconducteurs*. 2nd ed.; AbeBooks: Victoria, BC, Canada, 1975; pp. 1–728.
[30] Tsaousidou, M.; Butcher, P.N.; Triberis, G.P. Fundamental relationship between the Herring and Cantrell-Butcher formulas for the phonon-drag thermopower of two-dimensional electron and hole gases. *Phys. Rev. B* **2001**, *64*, 165304, https://doi.org/10.1103/physrevb.64.165304.
[31] Jacoboni, C.; Canali, C.; Ottaviani, G; Quaranta, A.A. A Review of Some Charge Transport Properties of Silicon. *Solid-State Electron.* **1977**, *20*, 77-89, http://dx.doi.org/10.1016/0038-1101(77)90054-5.
[32] Gallagher, B.; Gibbings, C.J.; Peppers, M.; Cantrell, D.G. The thermopower of Si inversion layers. *Semicond. Sci. Technol.* **1987**, *2*, 456–459, https://doi.org/10.1088/0268-1242/2/7/011.
[33] Flexpde. Finite element partial differential solver. Available online: https://www.pdesolutions.com/ (accessed on 4 Septebmer 2022).
[34] Esseni, D.; Abramo, A.; Selmi, L.; Sangiorgi, E. Physically based modeling of low field electron mobility in ultrathin single- and double-gate SOI n-MOSFETs. *IEEE Trans. Electron Devices* **2003**, *50*, 2445–2455, https://doi.org/10.1109/ted.2003.819256.
[35] Cassé, M.; Ghibaudo, G. Low Temperature Characterization and Modeling of FDSOI Transistors for Cryo CMOS Applications. In *Low-Temperature Technologies and Applications*. Editor Kazi, M.S.N., Eds.; IntechOpen: London, UK, 2022; pp. 1–24.
[36] Paz, B.C.; Cassé, M.; Haendler, S.; Juge, A.; Vincent, E.; Galy, P.; Arnaud, F.; Ghibaudo, G.; Vinet, M.; de Franceschi, S.; et al. Front and back channels coupling and transport on 28 nm FD-SOI MOSFETs down to liquid-He temperature. *Solid-state Electron.* **2021**, *186*, 108071, https://doi.org/10.1016/j.sse.2021.108071.
[37] Ghibaudo, G.; Kamarinos, G. Analyse des propriétés de transport électriques dans le SSI. Utilisation du pouvoir thermo-électriques. *Rev. Phys. Appl.* **1982**, *17*, 133.
[38] Asheghi, M.; Touzelbaev, M.N.; Goodson, K.E.; Leung, Y.K.; Wong, S.S. Temperature-Dependent Thermal Conductivity of Single-Crystal Silicon Layers in SOI Substrates. *J. Heat Transf.* **1998**, *120*, 30–36, https://doi.org/10.1115/1.2830059.
[39] Romanjek, K.; Lime, F.; Ghibaudo, G.; Leroux, C. New approach for the gate current source–drain partition modeling in advanced MOSFETs. *Solid-state Electron.* **2003**, *47*, 1657–1661, https://doi.org/10.1016/s003 8-1101(03)00180-1.